# A Shape-Changing Wheeling and Jumping Robot Using Tensegrity Wheels and Bistable Mechanism

Sydney Spiegel<sup>1</sup>, Jiefeng Sun<sup>1</sup>, and Jianguo Zhao<sup>1</sup>, Member, IEEE

Abstract—Tensegrity structures made from rigid rods and elastic cables have unique characteristics, such as being lightweight, easy to fabricate, and high load-carrying to weight capacity. In this paper, we leverage tensegrity structures as wheels for a mobile robot that can actively change its shape by expanding or collapsing the wheels. Besides the shape-changing capability, using tensegrity as wheels offers several advantages over traditional wheels of similar size, such as shock-absorbing capability without added mass since tensegrity wheels are both lightweight and highly compliant. We show that a robot with two icosahedron tensegrity wheels can reduce its width from 400 mm to 180 mm and simultaneously increase its height from 75 mm to 95 mm by changing the expanded tensegrity wheels to collapsed disk-like ones. The tensegrity wheels enable the robot to overcome steps with heights up to 110 mm and 150 mm with the expanded and collapsed configuration, respectively. We establish design guidelines for robots with tensegrity wheels by analyzing the maximum step height that can be overcome by the robot and the force required to collapse the wheel. The robot can also jump onto obstacles up to 300 mm high with a bistable mechanism that can gradually store but quickly release energy. We demonstrate the robot's locomotion capability in indoor and outdoor environments, including various natural terrains, like sand, grass, rocks, ice, and snow. Our results suggest that using tensegrity structures as wheels for mobile robots can enhance their capability to overcome obstacles, traverse challenging terrains, and survive falls from heights. When combined with other locomotion modes (e.g., jumping), such shape-changing robots can have broad applications for search-and-rescue after disasters or surveillance and monitoring in unstructured environments. A video of the robot can be found at https://youtu.be/8W4j3aqRA2w

Index Terms—Multimodal Robots, Tensegrity, Mechanism Design, Bistable Mechanism, Jumping Robots

### I. INTRODUCTION

Robots equipped with multiple locomotion modes are better suited for safely entering, exploring, and leaving environments, compared to robots only with a single mode. Therefore, these multimodal robots are increasingly used in emergency management applications, such as search and rescue after natural disasters like earthquakes or radiation monitoring after nuclear leakages. Their ability to traverse different terrains, such as moving over uneven surfaces, over fields of debris, or small pass-through gaps, make them particularly valuable. For example, consider a robot deployed to enter a disaster area and search for survivors. In this scenario, it might need to move quickly on level ground, navigate over rubble,

This work is partially supported by the National Science Foundation under Grant CMMI-2126039.

<sup>1</sup>Sydney Spiegel, Jiefeng Sun, and Jianguo Zhao are all with the Department of Mechanical Engineering at Colorado State University, Fort Collins, CO, 80523, USA. (e-mail: sydney.c.spiegel@gmail.com; J.Sun@colostate.edu; Jianguo.Zhao@colostate.edu)

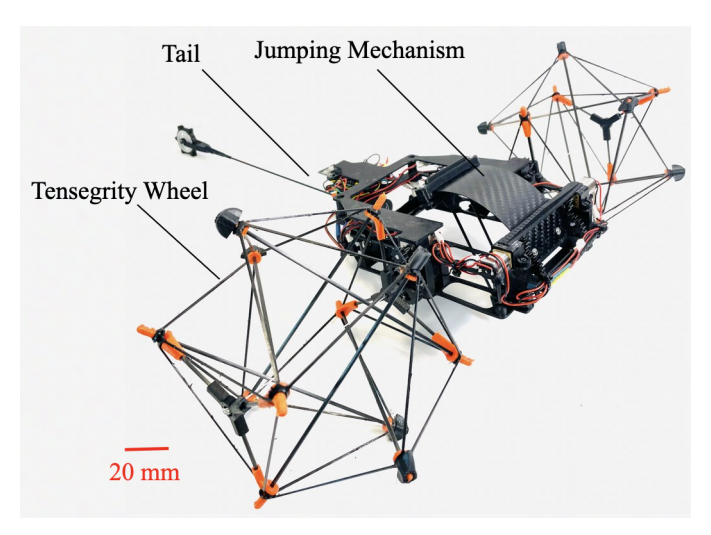


Fig. 1: The robot mainly consists of two tensegrity wheels and a bistable jumping mechanism. The approximate size is 500 mm (L)  $\times$  400 mm (W)  $\times$  100 mm (H).

pass through narrow gaps, and withstand potential falls from ledges.

This paper presents a multimodal robot with rolling and jumping capabilities (Fig. []) that can roll over hard and soft surfaces, climb obstacles of various heights, and jump as needed. The rolling function is enabled by two wheels made from tensegrity structures which can collapse to increase the robot's height but decrease its width. The jumping function is enabled by a bistable mechanism that rapidly releases stored energy. We briefly review relevant research in the following four areas: 1) mobile robots with irregular wheels; 2) mobile robots with shape-changing wheels; 3) wheeled robots with jumping capability; and 4) tensegrity robots. Due to space limitations, our review will not be exhaustive, but there are many interesting works in each area. We will highlight pertinent review papers when available.

Traditional round wheels are efficient for moving on hard, flat surfaces, but they struggle to overcome obstacles larger than the wheel's diameter. To address this limitation, researchers have developed robots with irregular wheels to improve their mobility over various terrains. A common approach is to replace round wheels with whegs, wheel-like legs similar to spokes. Using whegs enhances a robot's ability to climb over obstacles. Examples of whegs-equipped robots include: Mini-Whegs IV [I], Loper [2], insect-inspired Mini-Whegs that can climb steep surfaces [3], Rising STAR [4], and a wheg robot that can climb high steps [5].

In addition to irregular wheels, researchers have recently studied shape-changing wheels to overcome some of the limitations of round wheels. Shape-changing wheels can be round for traveling on flat terrain but can adapt to changing environments by morphing their shape. Methods for achieving shape-changing wheels include the use of linkages [6], origami [7], [8], or centrifugal-driven mechanisms [9]. A particularly interesting strategy is to transform between a wheg and a wheel, such as TurboQuad [10], WheeleR [11], RoVaLL [12], Trimode [13], QuadRunner [14], and others, with a comprehensive review available in [15].

Although whegs or shape-changing wheels can overcome larger obstacles than round wheels, their capacity to move over taller objects is still limited. To address this, researchers have developed hybrid robots that combine rolling or wheeling with jumping capabilities. Examples include Sumo robot from Parrot Inc. or Sand Flea from Boston Dynamics. Other researchers have developed rolling and jumping robots such as the Scout robot [16], a small wheg-based jumping robot [17], a jumping crawling robot with adjustable trajectory [18], a jumping rolling robot [19], a robot that can jump while rolling forward [20] and an energy-efficient jumping—crawling robot [21]. Generally, existing hybrid rolling and jumping robots have wheels or whegs with fixed sizes.

Since our robot uses tensegrity structures as wheels, we also briefly review some research on tensegrity robots with a comprehensive review available in [22]. Tensegrity structures are made from pure tension members (cables) and pure axial loaded compression (rods), allowing them to deform under external loads, absorb shocks and be constructed quickly [23]. These advantages have recently led researchers to develop various tensegrity robots for different locomotion modes, such as rolling [24], [25], swimming [26], hopping [27], and crawling [28].

In this paper, we present the design, analysis, and testing of a shape-changing robot capable of wheeling and jumping by using a pair of icosahedron tensegrity wheels and a bistable mechanism (Fig. [1]). The wheels are used for locomotion and can change their shape by switching between an expanded and a collapsed disc-like state. Collapsing the wheels reduces the robot's width and increases the ground clearance. With the tensegrity wheels, the robot can climb slopes up to 45 degrees, overcome stair heights of 150 mm, and move at speeds up to 0.36 m/s over various hard or soft terrains. We use a bistable mechanism to store and quickly release energy, enabling the robot to jump over 300 mm in height.

The primary contribution of this paper is using tensegrity structures as shape-changing wheels for mobile robots that can roll and change shape, an area that has been largely unexplored in literature. Our tensegrity wheel integrates the benefits of wheel-leg wheels (whegs), shape-changing wheels, and tensegrity structures. This unique combination enhances its climbing capabilities, enables shape modification, provides compliance and shock absorption, allows for a high payload-to-bodyweight ratio, and is lightweight relative to its size which is useful for small jumping robots. Furthermore, we have developed design guidelines for choosing important parameters (e.g., size) of tensegrity wheels to climb over steps. These guidelines rely

on mathematical models that predict the maximum step height a given tensegrity wheel can overcome in either its expanded or collapsed state. The guidelines also include a force analysis using finite element analysis to determine the force required to collapse a given tensegrity wheel.

The rest of this paper is organized as follows. In section II, we detail the robot design, including the tensegrity wheels, the bistable mechanism, the body and tail, and the embedded control system for the robot. Section III analyzes the force required to collapse the wheels and the maximum climbable step height for given tensegrity rod lengths. Section IV presents the experimental results for testing the robot. Finally, we discuss the implications and limitations of our research in section V.

# II. ROBOT DESIGN

In this section, we describe the design of the robot, which contains four major parts: 1) the collapsible tensegrity wheels, 2) the bistable jumping mechanism, 3) the body and tail, and 4) the embedded control system.

# A. Collapsible Tensegrity Wheels

We first describe the design and fabrication of the tensegrity wheel system, which includes three main parts: the tensegrity wheel, the mechanism to collapse the wheel, and the mechanism to drive the wheels.

Tensegrity wheel: We chose an icosahedron tensegrity structure as the wheel because it is a suitable symmetrical and collapsible tensegrity design that is lightweight, simple, and well-suited for rolling. As shown in Fig. 2(a), the structure is made from 6 rigid rods and 24 elastic cables, whose construction methods are widely available, examples include 29, 30. We have appended the structure with two hubs to ensure we can drive it as a wheel and collapse it on demand. Each hub (interior and exterior) connects to the end of three rods through compliant joints. The interior hub is connected to the robot body, while the exterior hub serves as an anchor for a cable that collapses the tensegrity. We have also added end-caps to each rod's end to generate sufficient friction force for wheeling on the ground.

The tensegrity wheel's various components are fabricated from a variety of materials. The six rods are made from 2 mm diameter round carbon fiber that is lightweight and stiff. The rod's length,  $l_r$ , can be customized to create differentsized wheels. Here, we use  $l_r = 130$  mm as an example of the fabricated tensegrity wheels for a medium-sized robot. The elastic cables are 3D-printed using a Prusa printer and made from a highly elastic thermoplastic polyurethane (TPU) filament (Ninja-flex 85A) with a rectangular cross-section (the dimensions are discussed in the next paragraph). The rod end-caps, with a length of 12 mm, are a 3D printed abrasion-resistant TPU (Cheetah 95A) that can be press fit into the carbon fiber rods. The wheel hubs comprise three parts: the central hub, three short carbon fiber rods (2 mm diameter) emanating from the central hub, and three compliant connectors that connect the short carbon fiber rods to the end of rods of the tensegrity. The central hub is 3D printed using carbon fiber enhanced filament (Nylon-X). One end of the

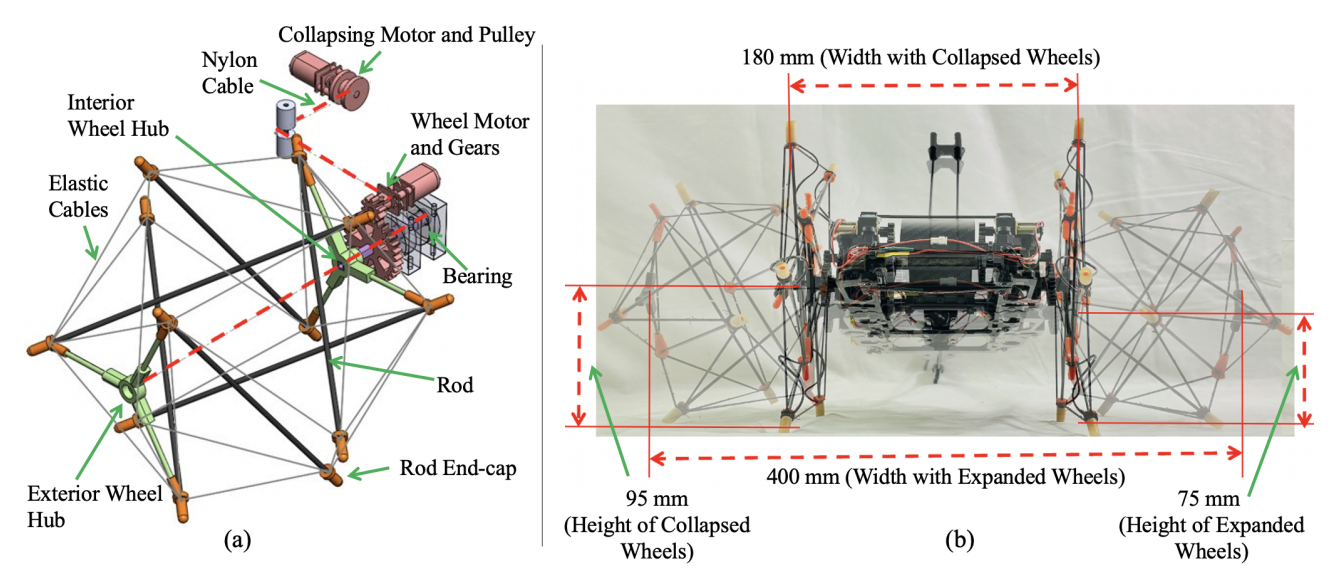


Fig. 2: The structure and results for the collapsible tensegrity wheels. (a) Schematic of driving and collapsing system for the tensegrity wheel (only half of the system is shown here since it is symmetric). (b) Collapsing the wheels can increase the robot's height and decrease its width.

three short carbon fiber rods is press fit into the central hub, and the other is press fit into the compliant connectors.

The tensegrity structure will be flat if the tension is too low but becomes spherical as it increases. If the tension is too high, the force required to collapse the tensegrity will necessitate a larger motor, leading to an unnecessary increase in the robot's weight (discussed in detail in section [III]). To generate a proper tension, the elastic cables are printed shorter than the distance  $l_c$  between the vertices of an ideal icosahedron tensegrity. For an ideal icosahedron tensegrity,  $l_c = 0.6l_r$  [31]. For an elastic cable 1.5 mm thick by 1 mm wide made with Ninja-flex 85 TPU, we choose a printed length of  $0.9l_c$  since this provides sufficient tension for a single wheel to hold the robot's weight (250 g) without collapsing.

Collapsing mechanism: To collapse the tensegrity wheel, we use a cable-driven system with a nylon cable that runs through the wheels to a pulley connected to a DC motor (collapsing motor in Fig. 2(a)). One end of the nylon cable is anchored at the center of the exterior hub; however, it can freely rotate to allow the wheel to collapse while rolling without twisting the cable. The cable runs through the open center of the wheel, then through the interior hub's center. It is then routed through a square hollow carbon fiber shaft, around the robot body, and finally attached to a pulley driven by a micro metal gear motor (Pololu: 1595) located at the rear part of the robot. As the pulley pulls the cable, the two wheels collapse from an expanded icosahedron into a flat disk-like shape. As shown in Fig. 2(b), collapsing the wheels decreases the robot's total width but increases its ground clearance (i.e., height). For a rod length of  $l_r = 130$  mm, the width decreases from 400 to 180 mm, and the ground clearance (measured from the ground to the center of the wheels) increases from 75 to 95 mm.

**Driving mechanism:** The driving mechanism for the two tensegrity wheels consists of a pair of micro metal gear motors

(Pololu: 4794) mounted to the robot's central frame. Each motor actuates a small 3D-printed nylon pinion that drives a larger gear (with a gear ratio of 3:1 to increase torque) attached to the hollow carbon fiber shaft, which is further attached to the interior hub's center. The shaft is mounted to the robot's body through two miniature bearings (Uxcell: 626-2RS), allowing for smooth rotations. The robot can thus move forward by rotating both motors in the same direction, and it can turn by rotating the motors in opposite directions.

### B. Jumping Mechanism

Our robot accomplishes jumping by utilizing a bistable mechanism with two stable states to store energy and quickly release it. A bistable mechanism is chosen because it requires fewer components and is a lightweight alternative to spring-actuated jumping mechanisms. Some designs based on bistable jumping mechanisms exist, such as a bistable robotic catapult [32], a compact jumping robot using snap-through buckling with twisting [33], and a composite sheet metal bistable mechanism [34]. The bistable mechanism in this paper is primarily based on the design proposed by Yamada et al. [35], which we select for its relative simplicity in implementation.

The working principle of our bistable jumping mechanism is briefly discussed as follows (Fig. 3). The mechanism contains a flexible plate, with its two ends attached to a passive and an active rotational joint, respectively. A jumping foot is attached to the flexible plate to push against the ground during the jumping process. Starting from the top bending configuration (state 1), when the active joint rotates the plate, it bends to store elastic energy. Upon passing through a critical configuration, the plate quickly snaps through, releasing the stored energy and causing the jumping foot to rapidly push against the ground for jumping (state 2).

To implement the jumping mechanism, we use a woven carbon fiber plate 145 (L)  $\times$  45 (W)  $\times$  0.3 mm (H). The

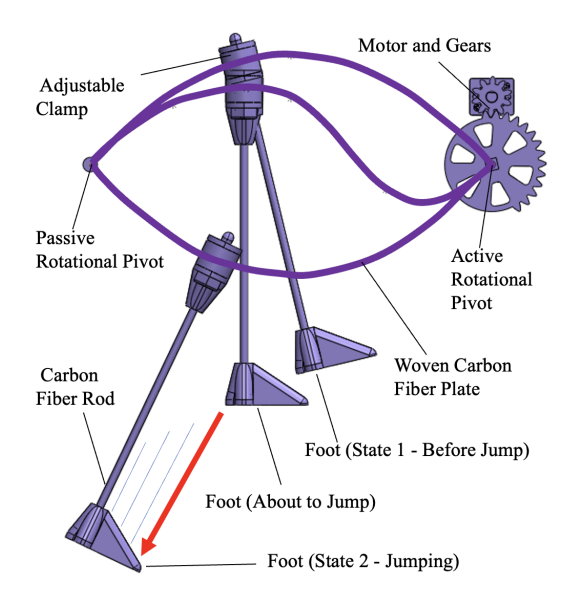


Fig. 3: Schematic of the bistable jumping mechanism's components and working principle.

active rotational joint is driven by a pair of micro metal gear motors (Pololu: 1595) mounted to the robot's central frame. Each motor drives a small nylon pinion that rotates a larger gear (gear ratio: 3:1) attached to a shared shaft. A pair of motors are used to keep the robot's design symmetrical and increase the torque. The larger gears have teeth removed to ensure that the woven carbon fiber plate will not be damaged by over-rotation from the active joint. The jumping foot is clamped over the carbon fiber plate, allowing its position to be adjusted along the plate so that the robot can take off at different angles to achieve different jumping performances. To enhance the friction between the foot and the ground, the foot is 3D printed from high-grip Ninja-Flex Edge filament (83A).

### C. Body and Tail Design

The robot body houses all the electronics, motors, and the bistable mechanism. As shown in Fig. 4, the body consists of 3D-printed Nylon top and bottom plates that enclose the bistable mechanism. The two motors for driving the wheels are placed on each side, the motor for collapsing the wheel is located at the rear, and the two motors for actuating the bistable mechanisms are placed at the front. Electronic components are distributed around the frame. The robot also has a tail made from a carbon fiber rod (2 mm diameter) with a small passive wheel (20 mm diameter) with six spurs at the tail's end. The 300 mm long tail serves two functions. First, it aids the robot in climbing over obstacles or up inclined slopes by acting as a compliant arm to support the robot's weight. Second, it assists the robot's jumping function by ensuring that, when the robot is at the apex of its jump, it will not fall and flip backward. Upon reaching the jump apex, the robot lands on its tail. The spurs on the tail wheel minimize slipping on smooth surfaces, enabling the robot to pivot about the tail wheel and fall forward from the full height of the tail.

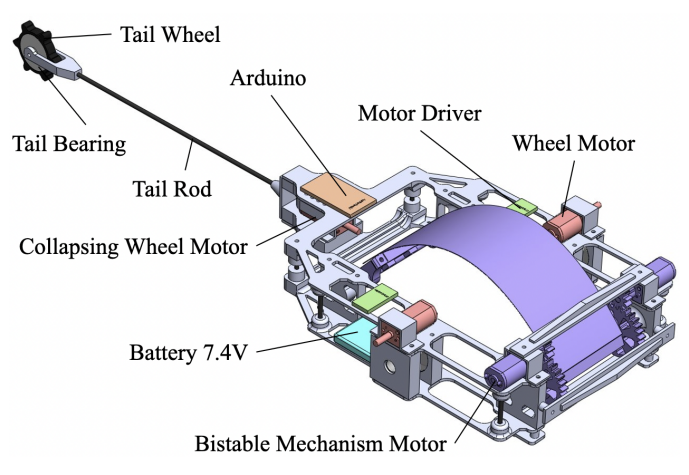


Fig. 4: Solid model of the robot's main body and tail.

# D. Embedded Control System

We aim to achieve untethered robot control by using an onboard embedded system. We choose the electronic components for the system to be as small and as lightweight as possible to maximize the jumping height. Therefore, only the necessary components to control the tensegrity wheels and jumping mechanism are used. A 7.4 V LiPo battery powers the whole system. An Arduino Pro Mini serves as the main controller. An infrared (IR) receiver (Uxcell: VS1838) allows for control of the robot via a remote. Two DRV8835 dual motor drivers (Pololu item: 2135) are used to control the five micro metal gear motors (two for driving, two for jumping, and one for collapsing).

# III. CHARACTERISATION AND MODELING

In this section, we analyze the critical functionalities of the tensegrity wheel to provide design guidelines for using tensegrity structures as wheels. First, we derive the force required to collapse a tensegrity wheel when important parameters, such as the width and thickness of elastic cables, are given. Then, we investigate the maximum step height the robot can climb for both the expanded and collapsed wheels, given the rod length  $l_r$ . We do not model or characterize the bistable jumping mechanism here since this has been extensively studied in previous works [35].

## A. Force Required to Collapse a Tensegrity Wheel

To select an appropriate motor and structural design for a tensegrity robot's wheel, it is crucial to know the force required to collapse the wheel. When the rod length is fixed, the collapsing force mainly depends on the property of the elastic cables (e.g., the initial pre-stretch and the dimensions for the cross-section). It is challenging to establish an analytical model because of the complex nature of the problem, such as the nonlinearity of the elastic cables and potential contact/slide between rods during the deformation. Therefore, finite element analysis (FEA) is utilized to determine the collapsing force with respect to the cable displacements.

To use FEA to analyze the force, we first experimentally obtain the force-displacement relationship for a single elastic

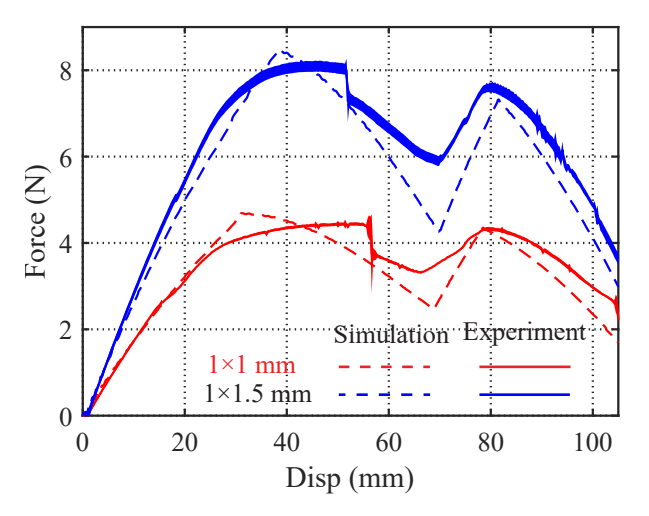


Fig. 5: Comparing the simulation and experimental results for the force-displacement relationship when collapsing a tensegrity wheel.

cable since its behavior (e.g., creep, hyper-elastic, etc.) is complex and cannot be easily modeled. We test two cables with different cross-section dimensions ( $1 \times 1$  mm and  $1 \times 1.5$  mm) using a test stand (Mark-10, M303) with an M5-2 force gauge. We first stretch the elastic cable to the same length as it would be on the expanded tensegrity (83 mm) and wait 10 minutes to remove the creeping effect in the TPU material. After that, we measure the force-displacement relationship by releasing or loading the cable (when a tensegrity wheel is collapsed, some elastic cables stretch while others relax) with a velocity of 0.85 mm/s. This velocity matches the velocity at which the elastic cables in the tensegrity wheel are stretched/relaxed when the wheel is collapsed, allowing us to cancel the influence of dynamic effects of the material such as creeping and damping.

With the experimental data for a single elastic cable, FEA is conducted using Abaqus (6.14, Dassault Systèmes) to predict the force-displacement relationship when the tensegrity wheel is collapsed. We use non-linear springs (CONN3D2) for the elastic cables and define the non-linear spring by using the experimentally obtained force-displacement relationship. The rods are modeled with beam elements (B31); the wheel hub is simplified to a rigid triangle (CONN3D2); the connection of the rigid hub and the rods is simplified as a spherical joint. Contact between the rods is created with "Edge-to-Edge" contact. The contact between rods is essential, as the tensegrity wheel cannot be compressed into a flat shape without contact. The simulation starts with a static step to let the pre-stretch come to a steady state, during which the pretension in the elastic cable will add load to the tensegrity structure. Then an implicit dynamic step with moderate damping is simulated. The simulation results are plotted as dashed lines in Fig. 5.

To validate the simulation results, we also experimentally obtain the force-displacement relationship for collapsing a tensegrity wheel. During the experiments, we fix one hub and compress the wheel using the same testing stand and force gauge. We conduct experiments for two tensegrity wheels with

elastic cables of the same dimensions used in the simulation. For each cable, the experiments are repeated three times. The results are plotted as solid lines representing the mean value in Fig. [5]. The results suggest a considerable reduction in the required force at a little over halfway through the collapsing process (60 mm). This reduction is due to some members applying a force in the direction of collapse after some rods contact each other.

As shown in Fig. 5, the simulated force with respect to the displacement has a similar shape to the experimental results. Furthermore, the predicted maximum force is only 5% off from the experimental result (8 N) for the tensegrity wheel using 1 x 1.5 mm cross-sectional TPU. The discrepancy might be due to the elastic cables' different moving (stretching or relaxing) speeds during the collapsing process: cables moving slower might have a creep effect. Due to the good accuracy in predicting the maximum force, the simulation can be used for wheels of different sizes.

Determining the maximum force during compression can help us to choose a proper motor to collapse the wheels. The tensegrity wheel attached to our robot uses the TPU cable with a cross-section of  $1 \times 1.5$  mm because these dimensions result in adequate tension in a single tensegrity structure to hold the robot's weight (250 g) without collapsing. Based on the experimental results from the tensegrity wheels used on the robot (1  $\times$  1.5 mm), a minimum of 16 N (8 N for each wheel) is required to collapse both tensegrity wheels. Therefore, we select a gear motor (Pololu item: 1595) with a continuous torque supply of 0.19 Nm, which can generate a force of 38 N when using a 10 mm diameter pulley. While only 16 N is required to collapse both wheels, much more force is needed on uneven terrain because the wheels must drag across the ground. Therefore, we choose a motor that can at least supply double the minimum required force.

# B. Maximum Climbable Step Height

We further analyze the maximum step height the tensegrity wheel can climb in either an expanded or collapsed state. Specifically, we aim to derive the height as a function of the rod length  $l_r$  in the tensegrity to guide the design of tensegrity wheels. This guideline can be used to design tensegrity wheels with a proper  $l_r$  for climbing specific heights. We investigate two cases of an expanded or collapsed wheel: steps with and without an overhang. For both cases, we derive the mathematical expressions for the maximum step height as a function of  $l_r$  based on the inherent geometry.

Maximum climbable height with expanded wheels: When the wheels are expanded, we obtain the maximum climbable height by projecting the 3D wheel onto a plane parallel to the wheel hubs to obtain a 2D view of the wheel as shown in Fig. 6. The projected lengths for all 6 rods and 12 end-caps are the same, known parameters. We denote them as  $l'_r$  and  $l'_e$ , respectively. In this projected 2D view, the whole wheel becomes a regular hexagon, with each vertex located at one end of each rod.

We first solve some parameters that can be used for both the cases with and without an overhang, such as the length of

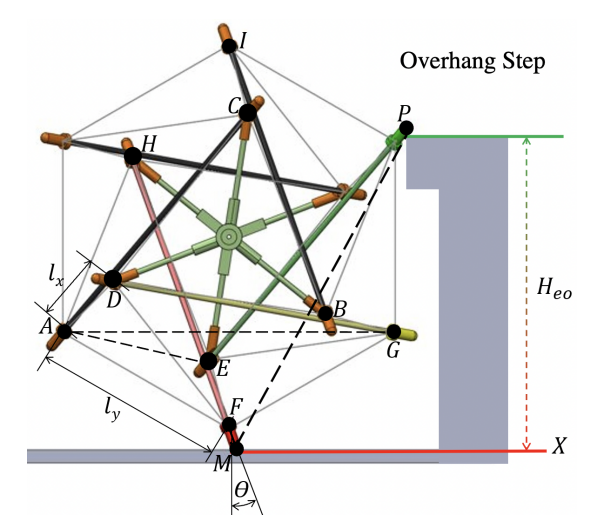


Fig. 6: The maximum climbable step height with an overhang. The height is achieved when the end-caps of rod EP and rod DG are aligned vertically which can only occur if the step has an overhang.

|AD|, denoted as  $l_x$ , and the length of |AF|, denoted as  $l_y$ . In  $\triangle AEF$  and  $\triangle ADG$ , we have the following two equations using the law of cosines:

$$l_y^2 = |AE|^2 + l_x^2 - 2|AE|l_x \cos(120^\circ)$$

$$|AG|^2 = l_x^2 + l_r'^2 - 2l_x l_r' \cos(120^\circ)$$
(2)

$$|AG|^2 = l_x^2 + l_r'^2 - 2l_x l_r' \cos(120^\circ)$$
 (2)

We can also solve  $|AE| = l_r'/2$  from  $\triangle ACE$ , and |AG| = $\sqrt{3}l_y$  from  $\triangle AFG$ . Plugging |AE| and |AG| into Eqs. (1) and (2), we can solve  $l_x = l_r'/4$ , and  $l_y = \sqrt{7}l_r'/4$ .

For the case with an overhang, the end of rod DG can freely rotate inside the overhang without contacting the step. This results in a configuration where the cable PG connecting rod EP and DG is vertical. To solve the climbing height, we need to solve |MP| and the  $\angle PMX$  to obtain the height as  $H_{eo} =$  $|MP|\sin \angle PMX$ . To solve  $\angle PMX$ , we first solve the angle  $\theta$  of the end-cap at point M with respect to the vertical line, which is equal to  $\angle HFI$ . In  $\triangle HFI$ , we have |HI| = |AE| = $l_r'/2,\ |FI|=2l_y,\ \text{and}\ |HF|=l_r'.$  Therefore, we can solve  $\theta=\arccos(|HF|^2+|FI|^2-|HI|^2/(2|HF|\times|FI|))=19^\circ.$ Then  $\angle PMX = 90^{\circ} - (\angle EMP - \theta)$ , where  $\angle EMP$  can be obtained in  $\triangle EMP$  using the law of sines. Finally, |MP| can be solved using the law of cosines in  $\triangle EMP$  with |EM| = $l'_r/4 + l'_e$ ,  $|EP| = l'_r + l'_e$ , and  $\angle MEP = 120^\circ$ . For the rod length  $l_r = 130$  mm and end-cap length  $l_e = 12$  mm, we have the projected length  $l'_r = 104$  mm and  $l'_e = 10$  mm. Plugging them into the equations, we can solve  $H_{eo} = 122$  mm.

For the case without overhang, the end of rod DG will contact the step first and push the wheel away, further rotating rod HF before rod EP touches the top of the step, which reduces the maximum step height that can be climbed. For rod EP to contact the step before rod DG, the step must be located at a distance no closer than the arc (shown in blue in Fig. 7) originating from M, the end of rod HF, and terminating at N, the end of rod DG. To obtain the maximum climbable height |PQ|, we can solve |MP| and |MQ|, respectively, and then |PQ| can be solved in the right triangle  $\triangle PQM$  as  $H_{en} =$ 

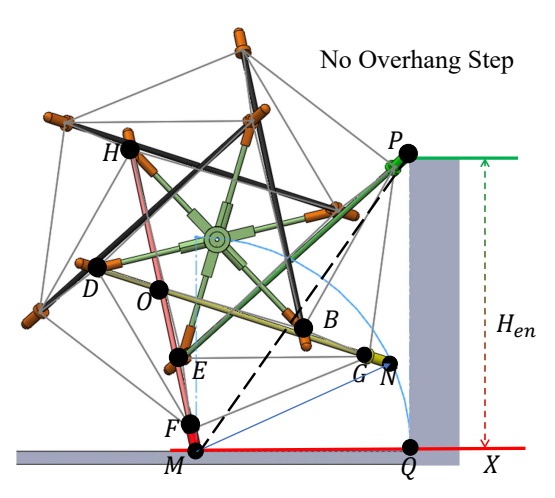


Fig. 7: The maximum climbable height for a step without an overhang.

 $\sqrt{|MP|^2 - |MQ|^2}$ . |MP| can be solved similarly to the case with an overhang by using the law of cosines in  $\triangle EMP$ . |MQ| = |MN|, which can also be solved by using the law of cosines in  $\triangle OMN$  with  $|OM| = |OF| + |FM| = l_r'/2 + l_e'$ and  $|ON| = |OG| + |GN| = 3l'_r/4 + l'_e$ . For  $l'_r = 104$  mm and  $l'_e = 10$  mm, we can solve |PQ| as  $H_{en} = 111$  mm.

Maximum climbable height with collapsed wheels: Surprisingly, when the wheels are collapsed, the resulting 2D shape is almost the same as the projected shape of the original 3D tensegrity. In this 2D shape, the lengths for the rod and endcap change to the original length,  $l_r$  and  $l_e$ , respectively. In this case, the analysis in the previous sub-section can be directly used by replacing  $l'_r$  with  $l_r$  and  $l'_e$  with  $l_e$ . For  $l_r = 130$  mm and  $l_e = 12$  mm, we can calculate the maximum height for the case with and without overhang to be, respectively,  $H_{co} = 149$ mm and  $H_{cn} = 138$  mm. The four predicted maximum climbing heights will be compared with experimental results in the next section.

Although we use  $l_r = 130$  mm in our design,  $l_r$  can be other values depending on the requirement. We believe it is best to keep  $l_r$  between 50 and 500 mm considering practical constraints from fabrication and the usage as a wheel. Additionally, while increasing  $l_e$  will also aid in overcoming obstacles, it also increases the difficulty to roll the tensegrity wheel, and longer end-caps will be more easily damaged. Therefore, we suggest keep  $l_e$  between 10 and 20 mm.

## IV. EXPERIMENTAL RESULTS

In this section, we present the experimental results for the developed robot, including wheeling, jumping, slope climbing, step climbing, and field experiments.

# A. Wheeling Test

Since a single icosahedron tensegrity will roll on the ground in a zig-zag fashion [23], we first investigate how a robot with two icosahedron tensegrity wheels will move on the ground and determine the step size for possible position control in the future. We built a simplified model by connecting two tensegrity wheels with a shared square shaft, which allows the wheels to roll in phase. To avoid other effects (e.g., slippage), we manually rotate the pair of wheels (see the supplementary video for the experiment). The results show that the two tensegrity wheels contact the ground with the same endcaps in a zig-zag fashion. But since the two wheels are symmetric with respect to the robot body, the robot moves forward linearly. From the experiments, the robot can move 86.6 and 99.6 mm per step for the expanded and collapsed wheel, respectively.

# B. Jumping Height Test

To optimize jumping height while clearing obstacles, the robot requires a steep takeoff angle. We performed jumping experiments to determine the optimal position of the jumping foot on the carbon fiber plate. For ease of testing, the foot was tested at four locations, corresponding to angles of 50, 60, 65, and 70 degrees relative to the robot's body, as shown at the bottom of Fig. 8.

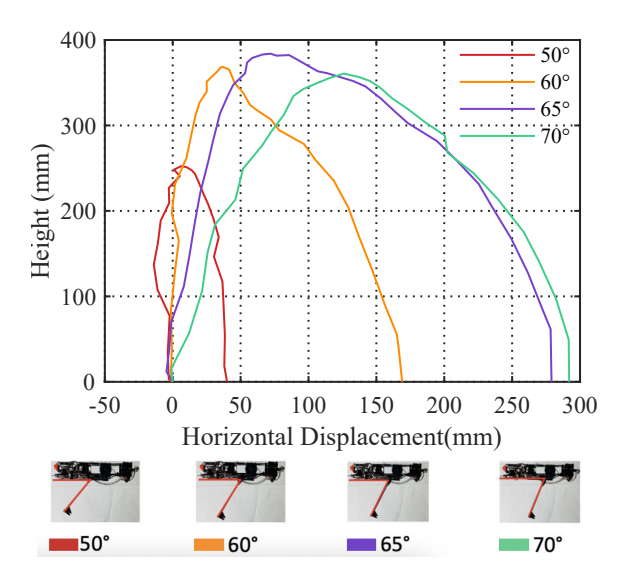


Fig. 8: Results for the max jumping height experiment showing the jumping trajectory (an average of three tests for each angle of the jumping foot ranging from 50 to 70 degrees as shown in the inset) of the center of the robot's wheel. The maximum height deviation for three repeated experiments is 3 mm.

For each jumping test, the robot was placed on a hard surface, and a marker was attached to the center of the wheel's hub to indicate the robot's position for tracking purposes. A video of the jump was recorded using an iPhone camera. The recorded video was then analyzed using video tracking software (Tracker), which can automatically track the attached sticker in the video to plot the robot's relative position as it jumped. Three jumping tests are conducted for each angle of the jumping foot, and the results are plotted in Fig. 8. From the figure, the maximum jumping height measured from the center of the robot's wheel is 384 mm, with the jumping foot at an angle of 65 degrees from the robot's body.

The robot can jump up to a height of 384 mm, but its maximum obstacle clearance is 300 mm due to the jumping foot below the robot body, as shown in the supplementary

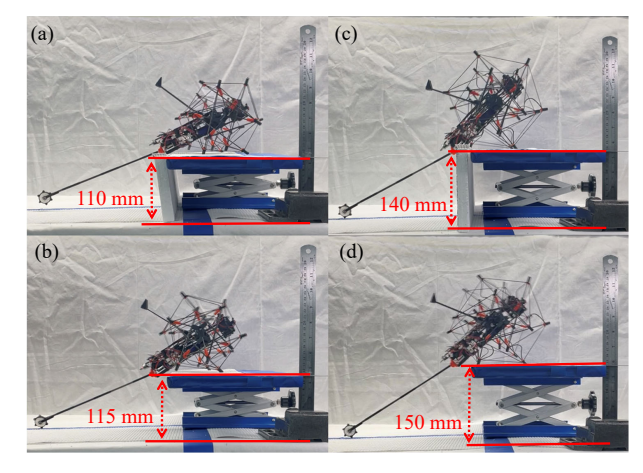


Fig. 9: Four different step-climbing cases were tested. (a) expanded wheels can climb a step with no overhang of 110 mm, (b) expanded wheels can climb a step with an overhang of 115 mm, (c) collapsed wheels can climb a step with no overhang of 140 mm, (d) collapsed wheels can climb a step with an overhang of 150 mm.

video. Nonetheless, the 300 mm obstacle jumping height is twice the maximum step height achievable with collapsed wheels, as depicted in Fig. 9.

# C. Inclined Slope Test

Climbing steep slopes is advantageous for robotic navigation in natural and urban environments. To determine the maximum slope the robot could climb using tensegrity wheels, we conducted the following experiment. First, the 7.4 V battery is fully charged before each test to ensure consistency between tests. Then, the robot was placed on a variable-degree angled slope made from thick foam with a high friction cabinet liner on top. We measured the static coefficient of friction between the tensegrity wheels and the high friction liner to be 0.78. This surface was chosen because it allowed the robot to climb a slope with minimal slipping. The slope angle was incrementally raised by 5-degree intervals until the robot could not ascend further. Notably, the robot ascended inclines up to 35 degrees without slippage. However, at a slope of  $\sim$ 40 degrees, slipping occurred, though the robot still managed to ascend. The maximum incline that the robot could climb was 45 degrees. A second test was conducted without the high grip liner, where the static coefficient of friction between the tensegrity wheel and polystyrene foam was measured to be 0.57. On this surface, the robot could only climb a slope of 40 degrees (see the supplementary video for the tests).

# D. Maximum Climbable Step Height Test

To validate our models in section III-B, we tested the maximum climbable step height for the expanded and collapsed wheels (each for the two cases with and without an overhang). We placed the robot on a flat surface with a variable height step (either with or without an overhang) in front of it. Then, the robot rolled forward until it encountered the step. The step height was increased between each test with an interval of 5

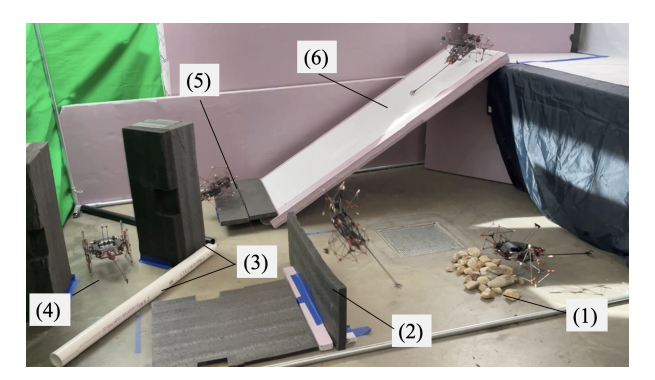


Fig. 10: An obstacle course was constructed to demonstrate the robot's ability to navigate different terrains, including (1) uneven rubble made from rocks, (2) a 250 mm tall wall, (3) loose round pipes, (4) a 200 mm wide gap, (5) a 100 mm tall step, and (6) an inclined ramp with a slope of 35 degrees.

mm (smaller size can be used, but we consider 5 mm is enough for comparing with our model prediction) until the robot could no longer climb up. The results are shown in Fig. 9, which validated our model prediction. Among all the four heights, only  $H_{eo}$  is 6% larger than the experimental result (predicted value is 122 with experimental value 115). This discrepancy is caused by the robot's front body getting stuck under the overhanging step when it is 120 mm tall.

### E. Field Experiments

To showcase the robot's capabilities in a single environment, we constructed an obstacle course, as shown in Fig. [10]. The course allowed the robot to locomote through different terrain features such as traversing a rock pile, jumping over a wall, climbing over loose round pipes, passing through a narrow gap, moving up a step, and climbing a ramp. In a single run, the robot could traverse through all obstacles.

We also conducted basic payload experiments on the robot as seen in Fig. [1] (b), during which we added liquid-filled bottles to the robot until it could no longer move forward. The robot can carry a payload of 1222 g, which is 4.9 times its weight, demonstrating its high load-carrying capacity.

Besides indoor tests, we further test the robot's performance in various outdoor real-world environments with some examples shown in Fig. [1] (see the supplementary video for the tests). We test the robot's ability to travel through different types of rocks, such as gravel (average grain size 2 mm), smooth river rocks, sharp rocks, coarse and fine sand, and vegetation (e.g., bush and tall grass). We also test the robot in winter conditions, including flat ice, ice with rocks (found in a frozen river), and snow. The one environment the wheel has the most difficulty traversing is forest floors with sticks as they would sometimes get stuck in the tensegrity wheels.

More experiments can be found in the supplementary video, including dropping the robot from 1.5 meters high to test the tensegrity wheels' shock-absorbing capability.

# V. DISCUSSIONS

We have demonstrated that using tensegrity structures as wheels for robotic locomotion exhibits several unique ad-

vantages. First, they are lightweight. The wheel with a rod length of 130 mm weighs 17 g, only 6.8% of the total weight of the robot. Second, they are easy to fabricate and inexpensive with carbon fiber rods and 3D-printed elastic cables. It only takes a few minutes to assemble a wheel from the rods and cables. Third, they can have the shapechanging capability between an expanded and a collapsed state to adapt to different environments. Fourth, they have good durability, enduring challenging terrains such as sand, rocks, concrete, ice, snow, and vegetation without significant signs of deterioration or damage. Despite undergoing 300 collapses during 12 months of use, the elastic cables retained sufficient tension. Nonetheless, we recognize that the 3D printed hub is a potential weakness in the current design, and its strength could be enhanced by incorporating higher-quality materials such as aluminum or injected-molded plastic.

Our developed models can also be used as guidance for others to design their own tensegrity wheels. The models for predicting the maximum climbable height can be first leveraged to determine the proper size of the tensegrity (e.g., rod length  $l_r$ ) given the obstacle size the robot needs to overcome. After determining the size, our FEA analysis can then be used to determine the force required to collapse the tensegrity so that a proper motor can be selected, and the robot's body structure strength can be appropriately designed.

Our work can be improved in the following aspects. First, the robot may sometimes fall sideways with the collapsed wheels, especially when it tries to climb over stairs, due to the two-wheeled configuration and the small thickness of the two wheels in the collapsed state. It can be solved using a fourwheeled configuration to stabilize the robot. Second, although an FEA model is developed to predict the collapsing force, an analytical model would be preferred to generate better design insights. We think such a model can be based on Castigliano's first theorem, which relates the strain energy, the displacement, and the force. By solving the potential energy in the tensegrity as a function of the displacement, we can then solve the force required to collapse the wheels. Finally, the current robot is manually controlled. We may consider adding additional sensors, such as cameras, GPS, or inertial measurement units, to perform localization and perception enable semi- or full autonomous operations. However, we may need to develop new algorithms for optimal path planning due to the robot's discrete motion and jumping capability.

# VI. CONCLUSIONS

This paper details the design, fabrication, and experimentation of a novel shape-changing tensegrity wheeled robot with a bistable jumping mechanism. As far as we know, this is the first work to use tensegrity as wheels for robotic locomotion. Tensegrity wheels are lightweight and easily fabricated. They can also be collapsed to increase the robot's height but decrease its width to change its size in different environments. Finally, they can serve as a shock-absorbing system to allow the robot to survive substantial falls. We also characterize and simulate the force required to collapse the tensegrity wheel and developed models to predict the maximum climbable



Fig. 11: (a) The robot can carry a payload of  $\sim$ 1222 g. (b) The robot can traverse a variety of outdoor terrain.

height for both the expanded and collapsed wheels. Together with a bistable jumping mechanism, we demonstrate that the developed robot can use its multimodal locomotion to traverse various indoor and outdoor environments, such as uneven, soft, and steep terrains. Based on the experimental results, we believe robots with tensegrity wheels will suit various applications (e.g., search and rescue) requiring a robot to traverse different and unstructured terrains.

### REFERENCES

- [1] J. Morrey, B. Lambrecht, A. Horchler, R. Ritzmann, and R. Quinn, "Highly mobile and robust small quadruped robots," in *Proceedings* 2003 IEEE/RSJ International Conference on Intelligent Robots and Systems (IROS 2003), vol. 1, 2003, pp. 82–87 vol.1.
- [2] S. D. Herbert, A. Drenner, and N. Papanikolopoulos, "Loper: A quadruped-hybrid stair climbing robot," in 2008 IEEE International Conference on Robotics and Automation, 2008, pp. 799–804.
- [3] K. A. Daltorio, T. E. Wei, A. D. Horchler, L. Southard, G. D. Wile, R. D. Quinn, S. N. Gorb, and R. E. Ritzmann, "Mini-whegs tm climbs steep surfaces using insect-inspired attachment mechanisms," *The International Journal of Robotics Research*, vol. 28, no. 2, pp. 285–302, 2009.
- [4] D. Zarrouk and L. Yehezkel, "Rising star: A highly reconfigurable sprawl tuned robot," *IEEE Robotics and Automation Letters*, vol. 3, no. 3, pp. 1888–1895, 2018.
- [5] X. Song, X. Zhang, X. Meng, C. Chen, and D. Huang, "Gait optimization of step climbing for a hexapod robot," *Journal of Field Robotics*, vol. 39, no. 1, pp. 55–68, 2022.
- [6] Y. She, C. J. Hurd, and H.-J. Su, "A transformable wheel robot with a passive leg," in 2015 IEEE/RSJ International Conference on Intelligent Robots and Systems (IROS), 2015, pp. 4165–4170.
- [7] D.-Y. Lee, S.-R. Kim, J.-S. Kim, J.-J. Park, and K.-J. Cho, "Origami wheel transformer: A variable-diameter wheel drive robot using an origami structure," *Soft robotics*, vol. 4, no. 2, pp. 163–180, 2017.
- [8] D.-Y. Lee, J.-K. Kim, C.-Y. Sohn, J.-M. Heo, and K.-J. Cho, "High-load capacity origami transformable wheel," *Science Robotics*, vol. 6, no. 53, p. eabe0201, 2021.
- [9] S. Ryu, Y. Lee, and T. Seo, "Shape-morphing wheel design and analysis for step climbing in high speed locomotion," *IEEE Robotics and Automation Letters*, vol. 5, no. 2, pp. 1977–1982, 2020.
- [10] W.-H. Chen, H.-S. Lin, Y.-M. Lin, and P.-C. Lin, "Turboquad: A novel leg-wheel transformable robot with smooth and fast behavioral transitions," *IEEE Transactions on Robotics*, vol. 33, no. 5, pp. 1025– 1040, 2017.
- [11] C. Zheng and K. Lee, "Wheeler: Wheel-leg reconfigurable mechanism with passive gears for mobile robot applications," in 2019 International Conference on Robotics and Automation (ICRA). IEEE, 2019, pp. 9292–9298.
- [12] J. V. S. Luces, S. Matsuzaki, and Y. Hirata, "Rovall: Design and development of a multi-terrain towed robot with variable lug-length wheels," *IEEE Robotics And Automation Letters*, vol. 5, no. 4, pp. 6017– 6024, 2020.
- [13] Q. Xu, H. Xu, K. Xiong, Q. Zhou, and W. Guo, "Design and analysis of a bi-directional transformable wheel robot trimode," in 2021 IEEE/RSJ International Conference on Intelligent Robots and Systems (IROS). IEEE, 2021, pp. 8396–8403.
- [14] A. Yeldan, A. Arora, and G. S. Soh, "Quadrunner: A transformable quasi-wheel quadruped," in 2022 International Conference on Robotics and Automation (ICRA). IEEE, 2022, pp. 4694–4700.

- [15] C. Zheng, S. Sane, K. Lee, V. Kalyanram, and K. Lee, "alpha-waltr: Adaptive wheel-and-leg transformable robot for versatile multiterrain locomotion," *IEEE Transactions on Robotics*, 2022.
- [16] S. Stoeter and N. Papanikolopoulos, "Kinematic motion model for jumping scout robots," *IEEE Transactions on Robotics*, vol. 22, no. 2, pp. 397–402, 2006.
- [17] B. Lambrecht, A. Horchler, and R. Quinn, "A small, insect-inspired robot that runs and jumps," in *Proceedings of the 2005 IEEE International Conference on Robotics and Automation*, 2005, pp. 1240–1245.
- [18] G.-P. Jung, C. S. Casarez, J. Lee, S.-M. Baek, S.-J. Yim, S.-H. Chae, R. S. Fearing, and K.-J. Cho, "Jumproach: A trajectory-adjustable integrated jumping-crawling robot," *IEEE/ASME Transactions on Mecha*tronics, vol. 24, no. 3, pp. 947–958, 2019.
- [19] J. Zhao, W. Yan, N. Xi, M. W. Mutka, and L. Xiao, "A miniature 25 grams running and jumping robot," in 2014 IEEE International Conference on Robotics and Automation (ICRA). IEEE, 2014, pp. 5115–5120.
- [20] K. Misu, A. Yoshii, and H. Mochiyama, "A compact wheeled robot that can jump while rolling," in 2018 IEEE/RSJ International Conference on Intelligent Robots and Systems (IROS). IEEE, 2018, pp. 7507–7512.
- [21] S.-H. Chae, S.-M. Baek, J. Lee, and K.-J. Cho, "Agile and energy-efficient jumping–crawling robot through rapid transition of locomotion and enhanced jumping height adjustment," *IEEE/ASME Transactions on Mechatronics*, 2022.
- [22] D. S. Shah, J. W. Booth, R. L. Baines, K. Wang, M. Vespignani, K. Bekris, and R. Kramer-Bottiglio, "Tensegrity robotics," *Soft robotics*, vol. 9, no. 4, pp. 639–656, 2022.
- [23] Z. Wang, K. Li, Q. He, and S. Cai, "A light-powered ultralight tensegrity robot with high deformability and load capacity," *Advanced Materials*, vol. 31, no. 7, p. 1806849, 2019.
- [24] A. P. Sabelhaus, J. Bruce, K. Caluwaerts, P. Manovi, R. F. Firoozi, S. Dobi, A. M. Agogino, and V. SunSpiral, "System design and locomotion of superball, an untethered tensegrity robot," in 2015 IEEE International Conference on Robotics and Automation (ICRA), 2015, pp. 2867–2873.
- [25] R. L. Baines, J. W. Booth, and R. Kramer-Bottiglio, "Rolling soft membrane-driven tensegrity robots," *IEEE Robotics and Automation Letters*, vol. 5, no. 4, pp. 6567–6574, 2020.
- [26] J. Shintake, D. Zappetti, T. Peter, Y. Ikemoto, and D. Floreano, "Bioinspired tensegrity fish robot," in 2020 IEEE International Conference on Robotics and Automation (ICRA). IEEE, 2020, pp. 2887–2892.
- [27] Y. S. Chung, J.-H. Lee, J. H. Jang, H. R. Choi, and H. Rodrigue, "Jumping tensegrity robot based on torsionally prestrained sma springs," ACS applied materials & interfaces, vol. 11, no. 43, pp. 40793–40799, 2019.
- [28] Y. Liu, X. Dai, Z. Wang, Q. Bi, R. Song, J. Zhao, and Y. Li, "A tensegrity-based inchworm-like robot for crawling in pipes with varying diameters," *IEEE Robotics and Automation Letters*, vol. 7, no. 4, pp. 11553–11560, 2022.
- [29] L.-H. Chen, M. C. Daly, A. P. Sabelhaus, L. A. Janse van Vuuren, H. J. Garnier, M. I. Verdugo, E. Tang, C. U. Spangenberg, F. Ghahani, A. M. Agogino, et al., "Modular elastic lattice platform for rapid prototyping of tensegrity robots," in *International Design Engineering Technical Conferences and Computers and Information in Engineering Conference*, vol. 58189. American Society of Mechanical Engineers, 2017, p. V05BT08A026.
- [30] M. Shibata, F. Saijyo, and S. Hirai, "Crawling by body deformation of tensegrity structure robots," in 2009 IEEE international conference on robotics and automation. IEEE, 2009, pp. 4375–4380.
- [31] S. D. Guest, "The stiffness of tensegrity structures," IMA Journal of Applied Mathematics, vol. 76, no. 1, pp. 57–66, 2011.

- [32] A. Yamada, M. Watari, H. Mochiyama, and H. Fujimoto, "A robotic catapult based on the closed elastica with a high stiffness endpoint and its application to swimming tasks," in 2008 IEEE/RSJ International Conference on Intelligent Robots and Systems, 2008, pp. 1477–1482.
- [33] A. Yamada, H. Mameda, H. Mochiyama, and H. Fujimoto, "A compact jumping robot utilizing snap-through buckling with bend and twist," in 2010 IEEE/RSJ International Conference on Intelligent Robots and Systems, 2010, pp. 389–394.
- [34] S.-P. Jung, G.-P. Jung, J.-S. Koh, D.-Y. Lee, and K.-J. Cho, "Fabrication of composite and sheet metal laminated bistable jumping mechanism," *Journal of Mechanisms and Robotics*, vol. 7, no. 2, p. 021010, 2015.
- [35] A. Yamada, H. Mochiyama, and H. Fujimoto, "Kinematics and statics of robotic catapults based on the closed elastica," in 2007 IEEE/RSJ International Conference on Intelligent Robots and Systems. IEEE, 2007, pp. 3993–3998.